Imaging issues for interferometric measurement of aspheric surfaces using CGH null correctors

Ping Zhou*, Jim Burge, Chunyu Zhao
College of Optical Science, Univ. of Arizona, 1630 E. Univ. Blvd, Tucson, AZ, USA 85721

ABSTRACT

Aspheric surfaces are measured using standard interferometers coupled with computer generated holograms (CGHs) that compensate the aspheric wavefronts. Such systems can measure complex aspheric shapes with accuracy of a few nanometers. However, the imaging properties of the interferometer-CGH combination can provide limitations for data mapping, resolution, and accuracy. These effects are explored, with an emphasis on the diffraction effects that are unique to interferometry.

Keywords: CGH, imaging aberration, transfer function, Talbot effect, phase smoothing, edge diffraction

1. Introduction

Aspheric optical surfaces are often tested using interferometers with the help of computer-generated holograms (CGHs), because CGHs can generate wavefronts of virtually any desired shape. The CGH is designed to transform a spherical wavefront from an interferometer to an aspheric one that matches the shape of the surface under test [1]. The CGH also performs another role. As an optical element, it relays the image of the surface under test to the interferometer.

The CGH is optimized for wavefront performance, and not for good imaging. The first order effect of imaging through CGHs is the mapping distortion. Mapping distortion can cause the lower order alignment error appear as high order wavefront errors. Interferometric measurement errors introduced by imaging distortion have been discussed in detail by Selberg, Murphy and Zhao [2-4].

The second order imaging aberrations due to the CGH can be described fully using field curvatures in the image that arise from the phase variations in the CGH. In general, the image will suffer defocus and astigmatism which vary across the focal plane. This aberration couples with diffraction to cause two principal problems with the measurement:

- Real errors in the surface will be blurred, which applies a low pass filter to the surface data. We treat this effect, which we call phase smoothing, as a function of the spatial frequency using a small-phase approximation to the well-known Talbot imaging relations.
- The combination of imaging aberrations and the amplitude discontinuity at edges shows up in the measurement as phase errors. We treat this effect using Fresnel integrals.

The field curves provide equivalent defocus projected into the two principal directions (S and T for an axisymmetric system). The two diffraction effects then have dependency on the orientation of the ripples or the edge with respect to the S and T directions. These are treated explicitly here using equivalent propagation distance and coordinate transformations.

A model for diffraction effects for refractive null correctors was developed by Zhao and Burge [5]. We further expand this to include the special issues with diffractive null correctors. We provide background for the diffraction effects for coherent systems such as interferometers in section 2. Section 3 presents a summary of the geometry and imaging aberration specific to CGH null testing of conic mirrors. The detailed derivations and analysis for this section are published by the authors elsewhere [6]. Section 4 presents the general method of coupling the diffraction effects with the imaging aberrations that arise from the use of CGHs. The specific example of null testing a 4.2-m diameter paraboloidal mirror is provided in Section 5.

Interferometry XV: Techniques and Analysis, edited by Catherine E. Towers, Joanna Schmit, Katherine Creath,
Proc. of SPIE Vol. 7790, 77900L · © 2010 SPIE · CCC code: 0277-786X/10/$18 · doi: 10.1117/12.862427

Downloaded from SPIE Digital Library on 29 Sep 2011 to 128.196.206.125. Terms of Use: http://spiedl.org/terms

2. Diffraction effects for coherent imaging systems

2.1. Interferometer imaging system

The imaging performance through the CGH is difficult to evaluate because it is part of a coherent system. For standard incoherent imaging, light is assumed to come from each point in the object and propagate in all directions. Some of the light makes it into the optical system, and is used for imaging. The aperture stop in the system defines which rays from the object will be used to create the image. If you change the stop, you change the imaging performance [5].

The imaging for most interferometers is fundamentally different. The light starts at a point source, and follows only refraction and reflection to the surface under test, then to the final image. The aperture stop in the system does not nominally define the light that makes it to the image. For this fully coherent system, it is convenient to think of one ray per point on the mirror. The ray will propagate to the image plane and define the image. Only for the case of large slope errors or high frequency ripple does the stop have any effect.

This fully coherent model leaves no room for imaging aberrations to degrade the image. Each ray will intersect the image plane at a sharp geometric point. We treat the imaging system using an infinitesimal bundle of rays, because when a ray hit a point with structures there is a bundle of rays coming out due to scattering and diffraction. These rays originate from each point on the surface under test. The width of the bundle can be defined in the computer model using the size of the stop at the focus in the interferometer. The stop, acting as a low-pass filter, limits the amount of the light that can make it to the detector.

Interferometer imaging aberrations are well known to degrade performance in other ways. Such aberrations cause "retrace errors" where large slope variations in the wavefront under test couple with aberrations to create phase errors that would result in an incorrect measurement [3]. This effect can be fully compensated if the aberrations are well known.

For incoherent imaging system, diffraction effects are washed out. For coherent imaging systems, diffraction effects influence interferometric measurements by smoothing actual phase irregularities and introducing phase errors due to edge diffraction.

2.2. Phase smoothing analysis using Talbot model

Diffraction effects cause a change in high spatial frequency components, which we call phase smoothing. Phase smoothing can be studied using the Talbot imaging theory [7, 8]. Talbot imaging is a diffraction phenomenon that occurs for any wavefront with a periodic complex amplitude. If a wavefront with complex amplitude of a period of d is illuminated by collimated light, then that same complex amplitude is formed by free space diffraction at integer multiples of the Talbot distance $z_T = 2d^2/\lambda$. As a sinusoidal phase pattern propagates, it will cycle through a reverse contrast amplitude pattern, a conjugate phase pattern, a pure amplitude pattern, then back to the original phase pattern.

If a wavefront with small phase ripples of W ($W << 1$) waves propagates a distance of L in collimated space, then the magnitude of the ripples will be attenuated to W'. A transfer function can be defined as

$$TF = \frac{W'}{W} = \cos\left(2\pi \frac{L}{z_T}\right) = \cos\left(\frac{\pi\lambda L}{d^2}\right), \qquad (1)$$

which can be used to predict the attenuation in high frequency (small scale) ripples due to propagation.

The Talbot distance z_T is defined for a collimated beam. For a spherical beam, it is convenient to convert it into an equivalent collimated beam and then use the Talbot effect to predict how wavefronts change due to propagation. The diffraction pattern for a spherical beam is the same as that observed for a collimated beam, except that the diffraction pattern occurs at the *effective propagation distance* L_e, and it is scaled in the transverse dimension.

Downloaded from SPIE Digital Library on 29 Sep 2011 to 128.196.206.125. Terms of Use: http://spiedl.org/terms

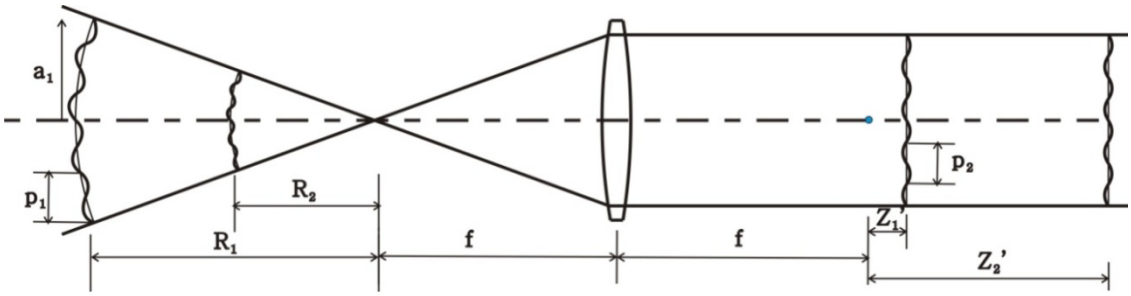

Figure 1. Propagation in a converging space is converted to equivalent propagation in a collimated space.

As shown in Figure 1, a converging wavefront starting with radius of curvature R_1 propagates to the position where it has a radius of curvature R_2, the effective propagation distance L_e can be defined as

$$L_e = \frac{R_1(R_1 - R_2)}{R_2}. \tag{2}$$

The effective propagation distance L_e can replace the propagation distance L in Eq. (2) to calculate the transfer function for the wavefront that propagates in a converging or diverging beam.

2.3. Edge effects using Fresnel integral

Edge diffraction from the test surface occurs when its edge is not in focus. The diffraction at the edge of the aperture can be modeled as the Fresnel knife-edge diffraction. The real and imaginary parts of the electric field distribution can be found by evaluating the Fresnel integrals [9]. Figure 2 shows the amplitude and phase fluctuations due to the edge diffraction. Both amplitude and phase have a rapid oscillation as the distance from the edge becomes large. The beauty of these pictures is that it works for any geometry and only scales with $\sqrt{\lambda L/2}$, where L is the defocus error in a collimated wavefront space or the equivalent propagation distance in a non-collimated wavefront space.

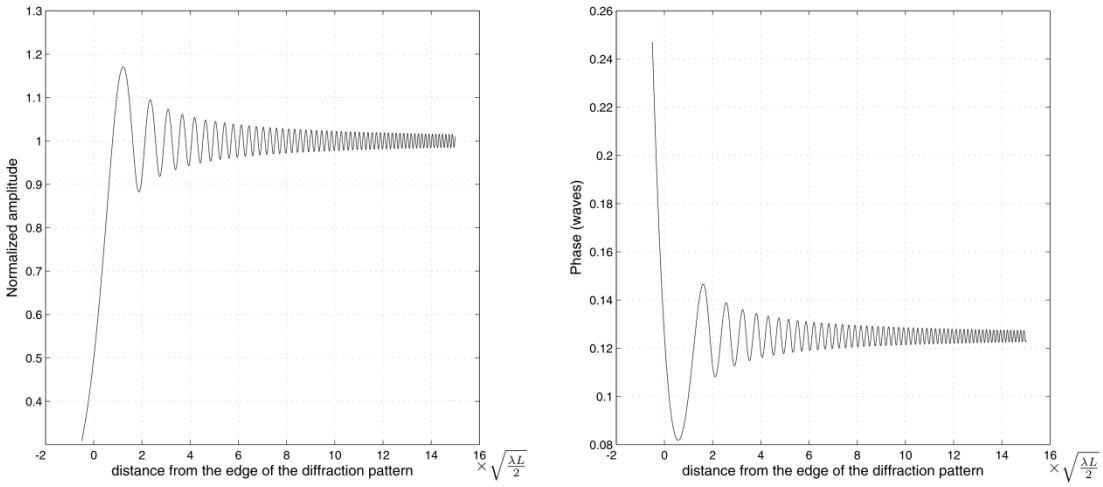

a) b)

Figure 2. The amplitude and phase variation calculated from the Fresnel integrals for the case of diffraction of collimated light from a knife edge.

The severity of effect of edge diffraction can be described by the *diffracted edge ratio*:

$$\varepsilon = \frac{5\sqrt{\lambda L/2}}{r_{image}}, \tag{3}$$

Downloaded from SPIE Digital Library on 29 Sep 2011 to 128.196.206.125. Terms of Use: http://spiedl.org/terms

where r_{image} is the image size in radius at the intermediate image. Here we arbitrary choose $5\sqrt{\lambda L/2}$ to calculate the diffracted edge ratio, which corresponds to about six ripples from the edge. For example, if the intermediate image is 50 mm in radius and it is 790 mm out of focus, then the diffracted edge ratio is 0.05 for the wavelength of 633 nm. Almost all of the edge effect occurs in the outer 5% of the radius. The phase error due to the edge diffraction is 3.7 nm as shown in Figure 3.

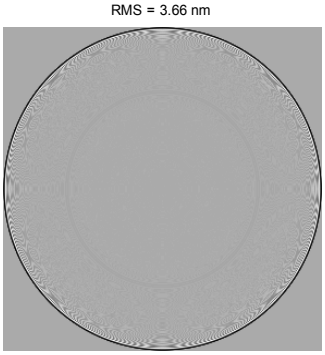

Figure 3. Phase error caused by edge diffraction. The diffracted edge ratio is 5% and the RMS phase error is 3.7 nm.

3. Interferometric measurements of aspheric mirrors using CGH null correctors

3.1. Test geometry

Here, we apply the results from a generalized model and analysis for CGH testing of conic mirrors [10]. Figure 4 shows the geometry of CGH null test for a conic surface. The hologram is placed distance *h* away from the paraxial center of curvature to avoid the caustic area. The CGH uses the power carrier to separate diffraction orders, and the light focuses at the point E. The phase function of the CGH is derived using this geometrical model. This model is constructed by computing the absolute path length along the direction of propagation. A ray that is perpendicular to the test surface is traced to the hologram and then to the focus point E.

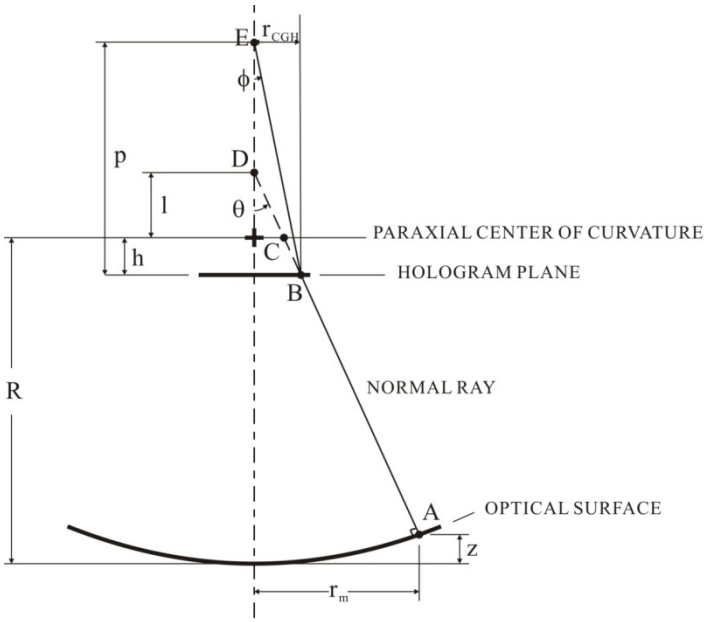

Figure 4. Test geometry using a hologram to test a conic surface. The hologram uses power carrier to separate the unwanted diffraction orders.

Downloaded from SPIE Digital Library on 29 Sep 2011 to 128.196.206.125. Terms of Use: http://spiedl.org/terms

The conic optical surface is given by

$$z(r)=\frac{r_m^{\,2}}{R+\sqrt{R^2-(K+1)r_m^{\,2}}}, \tag{4}$$

where r_m is the radial position on the test surface, R is the radius of curvature and K is conic constant. The phase function of the CGH is described by geometry, and approximated to the fourth order:

$$\begin{aligned}\Phi(r_m) &= (R-h)+p-\mathrm{AB}\text{-}\frac{p}{\cos(\phi)} \\ &= \frac{\left(-h^2+hp\right)r_m^2}{2pR^2}+\frac{\left(h^4-4h^2p^2-4h^2Kp^2+3hp^3+4hKp^3+4hKp^2R-3Kp^3R\right)r_m^4}{8p^3R^4}\end{aligned}. \tag{5}$$

3.2. Imaging distortion

The first order effect of imaging through CGHs is the mapping distortion, which means the mapping from the test optic to the interferogram is not linear. Null correctors are optimized to generate an aspheric wavefront but not necessarily to provide uniform mapping from the test optic to the image plane. The imaging distortion from a null corrector will cause three complications: one is that the surface defects appear shifted; the second is that lower order alignment errors appear as higher order wavefront errors; the third problem is that diffraction effects, which depend on spatial frequency, will vary as the magnification changes with position and orientation.

For an axisymmetric system, the mapping distortion between the radial position on the mirror r_m and the radial position on the CGH r_{CGH} is approximately

$$r_{\mathrm{CGH}}(r_m)=a_1 r_m + a_2 r_m^{\,3}, \tag{6}$$

where a_1 and a_2 are constant, and are related to the magnification and distortion.

Mapping distortion also causes the nonlinear magnification in the radial and circumferential directions. We define the magnification in polar coordinates, with ϕ as the polar angle and α as the azimuthal angle. The radial magnification to polar coordinates $d\phi/dr_m$ be described as

$$\frac{d\phi}{dr_m}=\frac{d\phi}{dr_{\mathrm{CGH}}}\frac{dr_{\mathrm{CGH}}}{dr_m}=c_0+c_1 r_m^{\,2}, \tag{7}$$

and the circumferential or azimuthal magnification to polar coordinates is

$$\frac{r_{\mathrm{CGH}}\,d\alpha_{\mathrm{CGH}}}{r_m\,d\alpha_m}=\frac{r_{\mathrm{CGH}}}{r_{\mathrm{m}}}=c_0+c_2 r_m^{\,2}, \tag{8}$$

where c_0, c_1, c_2 are constants and they are related to the test geometry and the parameters of the conic surface.

3.3. Field curves

We determine the field curvatures from the two second derivatives for the axisymmetric hologram phase function Φ. One is in the radial direction C_t and the other C_s is in the circumferential direction, perpendicular to the radial direction. The two curvatures in the hologram coordinates are

$$\begin{aligned}C_t(r_m) &= \frac{d^2\Phi}{dr_{\mathrm{CGH}}^{\,2}}=\frac{d^2\Phi}{dr_{\mathrm{m}}^{\,2}}\cdot\left(\frac{dr_m}{dr_{\mathrm{CGH}}}\right)^2-\frac{d\Phi}{dr_{\mathrm{m}}}\frac{d^2r_{\mathrm{CGH}}}{dr_m^2}\left(\frac{dr_m}{dr_{\mathrm{CGH}}}\right)^3 \\ C_s(r_m) &= \frac{1}{r_{\mathrm{CGH}}}\frac{d\Phi}{dr_{\mathrm{CGH}}}=\frac{1}{r_{\mathrm{CGH}}}\frac{d\Phi}{dr_{\mathrm{m}}}\cdot\frac{dr_m}{dr_{\mathrm{CGH}}}\end{aligned}. \tag{9}$$

The two principal curvatures C_t and C_s bring the light to the tangential and sagittal focal planes for the axisymmetric system. This can be confusing because the "tangential focus" by this definition comes from curvature in the radial direction and the "sagittal focus" comes from the curvature in the circumferential direction. We maintain the "T" and

Downloaded from SPIE Digital Library on 29 Sep 2011 to 128.196.206.125. Terms of Use: http://spiedl.org/terms

"S" definition for the field curves, but refer to C_t as the radial curvature and C_s as the circumferential curvature. This is illustrated in Figure 5.

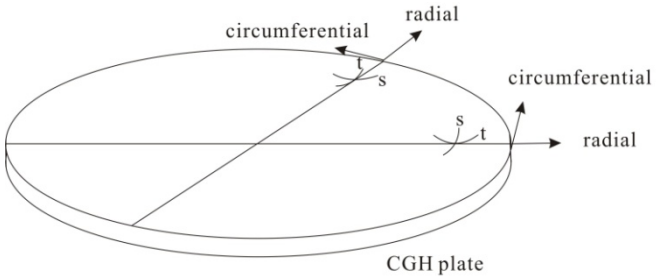

Figure 5: A sketch of the tangential and sagittal curvatures for an axisymmetric hologram.

When a small bundle of rays originating from a point on the test surface are incident on the hologram, the rays see different curvatures. The fans in the radial and circumferential directions will focus onto separate curved surfaces because of the field curvature and astigmatism imaging aberrations from the CGH. These field curvatures can be obtained in commercial raytracing software or calculated by using generalized Coddington equations [11]. The generalized Coddington equation for diffractive optics is

$$\begin{aligned} \frac{\cos^2\phi}{t'} - \frac{\cos^2\theta}{t} &= C_t \\ \frac{1}{s'} - \frac{1}{s} &= C_s \end{aligned}, \tag{10}$$

where t and s are the physical distance from the test surface to the hologram, and t' and s' are the distance from the hologram to the tangential image point and sagittal image point.

To evaluate the coupling of diffraction with the field curvature, we create an image at an equivalent collimated space by inserting an ideal lens with a focal lens of f at one focal length away from the point focus. This construction is useful because it simplifies the analysis, but it is not necessary. The focal length itself is arbitrary, and will be normalized out of the result. An ideal lens preserves the field curves and creates a collimated wavefront, and telecentric image. We show elsewhere that the equivalent propagation distance in collimated space maintains the diffraction performance for general converging or diverging light [8].

When the distance between the hologram and the paraxial focus h and the distance between the hologram and the point focus p are small compared to the radius curvature of the test piece R, the field curves are mostly quadratic in field. We can use the geometric imaging relationship to calculate the field curves. Keeping the dominant quadratic terms, the two field curves are

$$\begin{aligned} t_i' &\approx \frac{3f^2K}{2p^2R} r_m^{\,2} \\ s_i' &\approx \frac{f^2K}{2p^2R} r_m^{\,2} \end{aligned}. \tag{11}$$

For axisymmetric surface, the inside and outside edges are always circumferential, which means the diffraction effects from the edge is always radial and caused by the T-component of the field curves. We can use the field curves to analyze the phase ripple and edge effects in the principal radial and circumferential directions. For non-axisymmetric surface, the boundary could be in general directions, so the diffraction calculation must use the combination of the two field curves.

Downloaded from SPIE Digital Library on 29 Sep 2011 to 128.196.206.125. Terms of Use: http://spiedl.org/terms

4. Coupling of diffraction effects with field curves

Fundamentally, the field curves show defocus in the image space as functions of field position and orientation. The diffraction effects can be treated at each field point and orientation as propagation of light from its focused position given by the field curve to the focal plane. This is apparent for the principal S and T orientation. The case with general orientation is provided elsewhere [5,6].

We simplify the problem using the concept of ideal lenses to transfer from one plane to another. If the wavefront ripples are imaged correctly from one space to another, there is no attenuation from the Talbot effect. The magnitude of the amplitude and phase ripples will be preserved. For the plane that is out of focus, the Talbot effect described above can be used to determine the change in phase due to the propagation. In any re-imaged optical space, the propagation distance equals to the out of focus distance. The spatial period of the ripples must correctly include the magnification of the image.

The same principle applies for the field curves, but this includes variation across the image of the test surface and it includes a defocus in the circumferential and radial directions. The defocus across the field is given by the field curves, and the two curves correspond to the image with ripples that are radial or circumferential. Interferometers can only focus one plane at a time so that the other field will be out of focus.

To evaluate the phase smoothing effect at an arbitrary image plane, we use the fact that the longitudinal magnification in distance and transverse magnification of the spatial period cancel with each other. If we relay the image with a local magnification m, the spatial periods of the wavefront ripples d will be magnified by m. Assuming the field curvatures are not corrected by the intermediate optics, the amount of defocus for any field point is given by the longitudinal magnification, which is equal to m^2. The effect of propagation, as seen in the transfer function, is invariant to magnification:

$$TF = \frac{W'}{W} = \cos\left(\frac{\pi\lambda z_1}{d_1^{\,2}}\right) = \cos\left(\frac{\pi\lambda m^2 z_1}{(md_1)^2}\right) = \cos\left(\frac{\pi\lambda z_2}{d_2^{\,2}}\right). \tag{12}$$

Note that both the magnification m and z_2 in the above equation vary across the field. They are a function of position and orientation. The radial and circumferential magnifications are given in Eq. (7-8). This means that we can evaluate the wavefront smoothing at any intermediate imaging space and the result will be the same. If d_1 and z_1 are in the space of the test surface, then we can normalize the period d_1 with the test surface size $2a$ and the transfer function becomes

$$TF(r_m) = \cos\left[\frac{\pi\lambda z_2(r_m)}{m(r_m)^2 d_1^2}\right] = \cos\left[\frac{\pi\lambda z_2(r_m) f_{\text{normalized}}^2}{4a^2 m(r_m)^2}\right] \tag{13}$$

The normalized frequency has a unit of cycles/diameter. The transfer function depends on the field curves and the local magnification at each field point.

This transfer function is given for the principal orientations, radial and circumferential for the axisymmetric CGH. The development of the transfer function for sinusoidal ripples in an arbitrary direction is provided elsewhere [6].

The non-linear mapping from the CGH creates distorted imaging where features near the edge of the mirror are proportionally larger. The difficult for optical testing comes about near the center where the actual features are greatly de-magnified. A constant frequency at the mirror will appear to have higher frequency variation near the center.

5. Example

In this paper, we use a 4.2 m parabola with a radius of curvature of 16 m as an example to look at its imaging performance. The CGH is placed 225 mm below the paraxial focus ($h = 225$ mm), and the point focus after the CGH is 480 mm above the hologram ($p = 480$ mm). The CGH is 95 mm diameter. Its phase function is shown in Figure 6. We expand the phase function into the Taylor series in r_m to the order r_m^6, which matches the exact phase function well. Using the truncated Taylor series can simplify the field curvature calculation.

Downloaded from SPIE Digital Library on 29 Sep 2011 to 128.196.206.125. Terms of Use: http://spiedl.org/terms

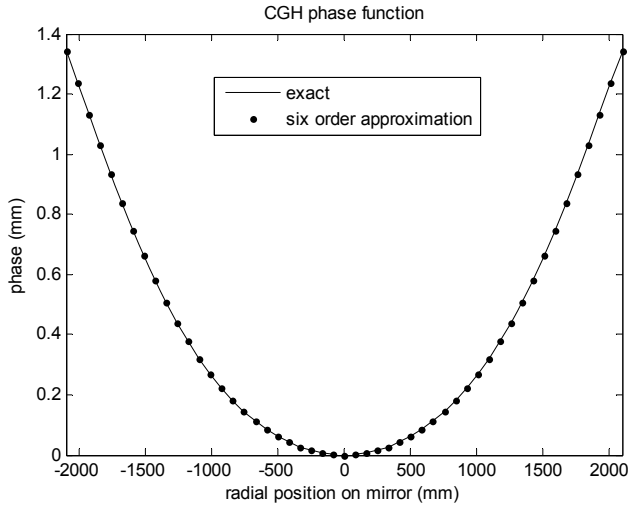

Figure 6. The CGH phase: exact form and r^6 approximation. This plot is for a CGH used to test a 4.2 m parabola with a radius of curvature of 16 m. The CGH is place 225 mm below the paraxial focus, and the point focus after the CGH is 480 mm above hologram.

The image distortion from the test surface to the CGH is defined by the mapping shown in Figure 7.

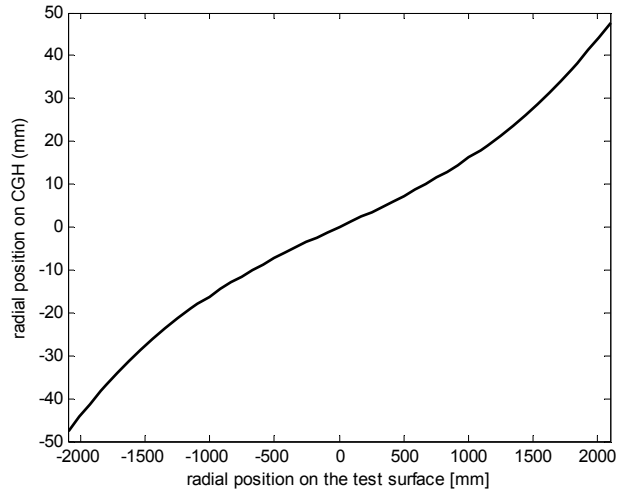

Figure 7. CGH mapping function showing the relationship between the test surface position and position on hologram.

The radial curvature C_t and the circumferential C_s curvatures, defined as directional derivatives of the phase function are given in Figure 8.

Downloaded from SPIE Digital Library on 29 Sep 2011 to 128.196.206.125. Terms of Use: http://spiedl.org/terms

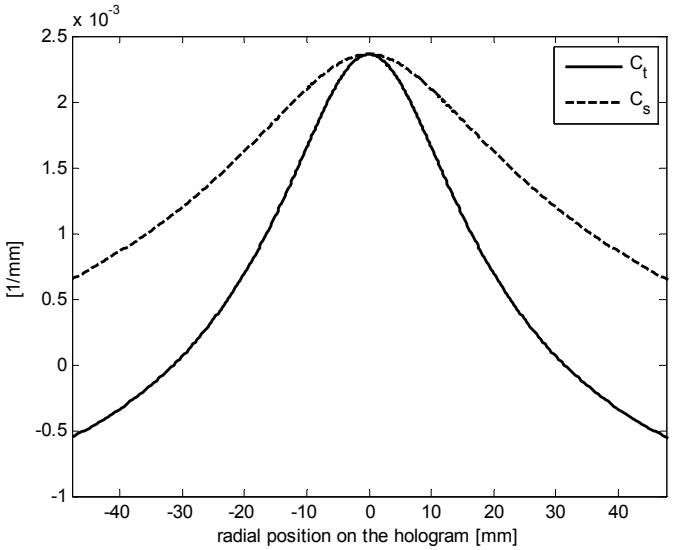

Figure 8. The radial C_t and the circumferential C_s curvatures for the CGH used to test the 4.2-m paraboloidal mirror for the case where the CGH position is 225 mm below the paraxial focus, and the point focus after the CGH is 480 mm above the hologram.

To treat the hologram as coherent imaging system, we model the parabola as the object, and its field is from -2100 mm to 2100 mm. The aperture stop is located at the point image of the interferometer. Figure 9 shows a ray trace model by Zemax. The software must have "ray aiming" turned on so the ray bundles will be correctly defined by this stop, and the stop size is 1 mm diameter, which passes slopes up to 31.25 μrad and spatial frequencies up to 207 cycles/diameter. An arbitrary paraxial lens with a focal length of 200 mm is placed 200 mm away from the point focus to image the test surface through the hologram so that the wavefront is in a collimated space. The paraxial lens can be assumed to have an ideal imaging and will not introduce field curves. The paraxial lens was verified to faithfully reproduce the field curves. In an actual interferometric measurement, the optics inside the interferometer will act as this paraxial lens and re-image the field curves to the detector plane. The optics inside the interferometer may not be perfect and can cause additional aberration, but in this paper we consider only field curves introduced by the hologram.

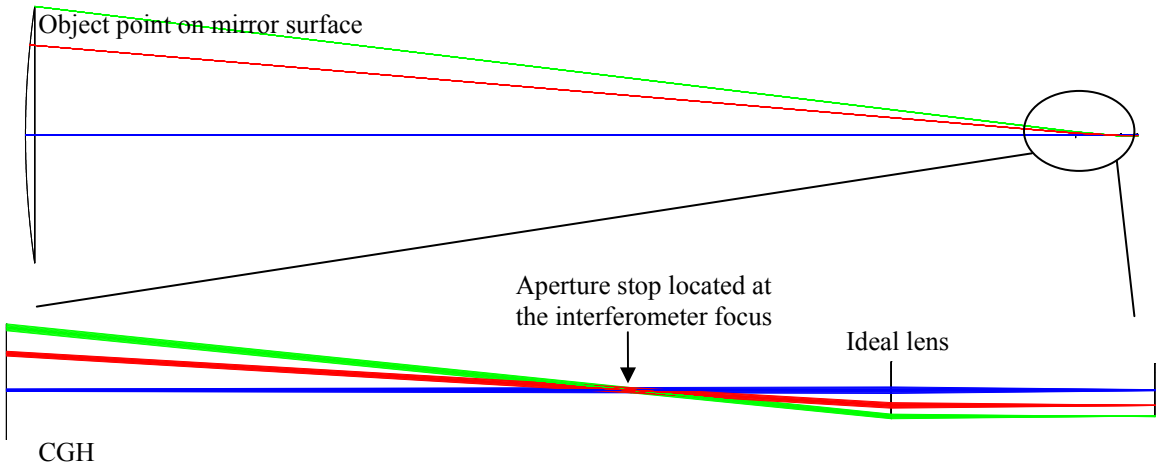

Figure 9. Layout of a null test for a parabola with a paraxial lens to create an equivalent collimated wavefront space.

If we choose the paraxial lens with a focal length of 200 mm, the field curves are shown in Figure 10. The difference between the T and S field curves at the full field is 46 mm as calculated in Zemax.

Downloaded from SPIE Digital Library on 29 Sep 2011 to 128.196.206.125. Terms of Use: http://spiedl.org/terms

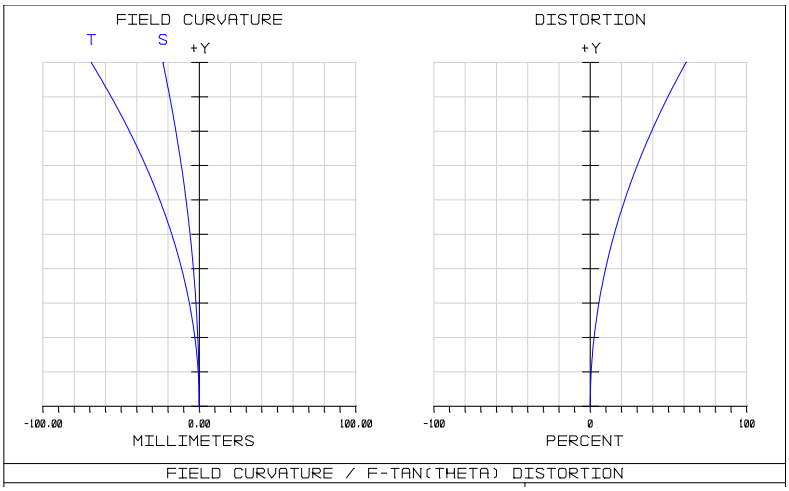

Figure 10. The field curves with the use of a paraxial lens with the focal length of 200 mm.

The radial and circumferential magnifications due to the CGH mapping distortion are shown in Figure 11.

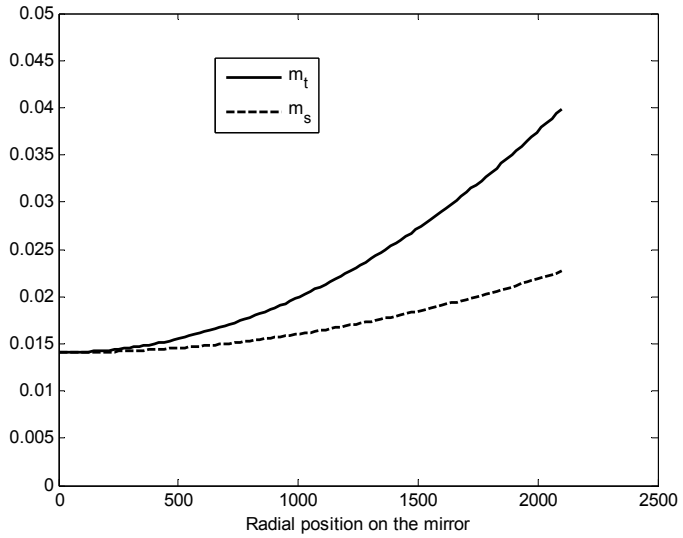

Figure 11. The radial and circumferential magnifications for the CGH used to test 4.2-m parabola with the radius of curvature of 16 m. The CGH is placed 225 mm below the paraxial focus of the parabola.

The effects of diffraction couple both the equivalent propagation given by the field curves and the variation in spatial frequency, given by the magnification. The performance is also clearly a function of the choice of focus, which is achieved in hardware by shifting the detector array. We illustrate these issues with the example of the 4.2 m parabola. We evaluate the diffraction effects by setting the focus at three different places: radial focus at the inside edge of the mirror, 600 mm from the center, focus at the outer edge, and halfway between. This is illustrated in Figure 12. When the interferometer focuses at the inner edge, the T curve at 600 mm field is in focus and the others are not.

Downloaded from SPIE Digital Library on 29 Sep 2011 to 128.196.206.125. Terms of Use: http://spiedl.org/terms

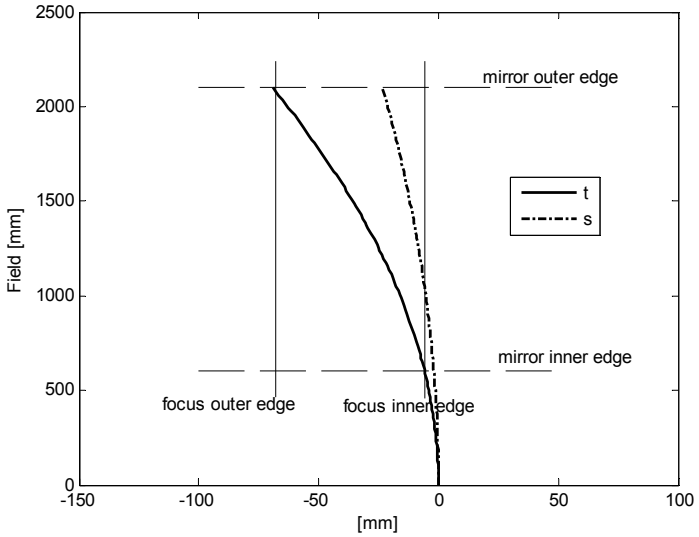

Figure 12. The field curves at the intermediate image plane. We could choose to set the interferometer at the inner edge of the mirror, defined by the central hole, at the outer edge, or any place between.

The transfer functions for phase ripples at the outer edge in radial and circumferential directions are shown in Figure 13(a). There is not much smoothing effect at the outer edge in both diffractions because even though the outer edge is out of focus for both S and T, the spatial ripples are greatly magnified, and the smoothing goes as the fourth power of spatial frequency. When the interferometer focuses at the outer edge of the test surface (at the full field of tangential field curve), the TF functions at the inner edge are given in Figure 10(c). This is considerably worse. We also show a case halfway between the two.

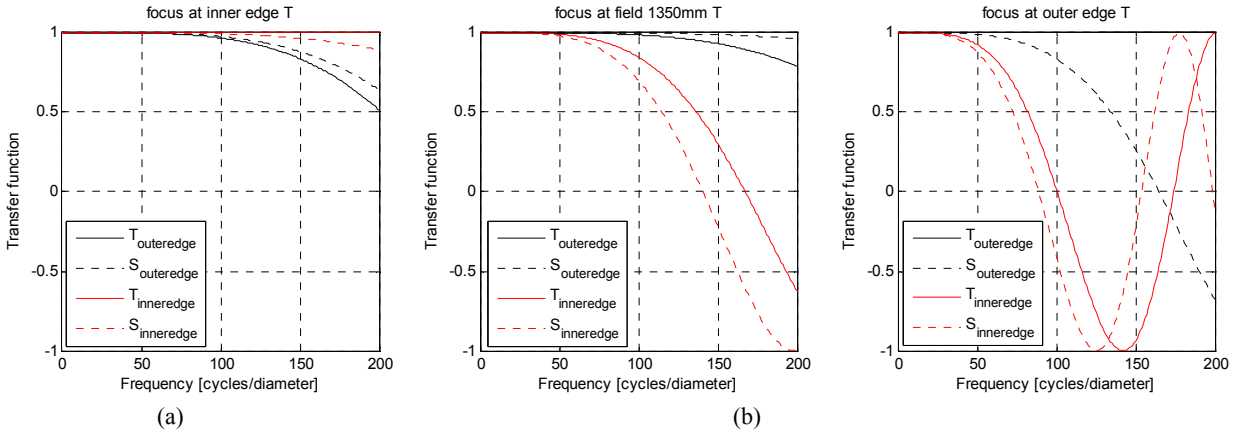

Figure 13. Transfer functions: a) the interferometer focuses at the inner edge of the mirror; b) the interferometer focuses at the field 1350mm; c) the interferometer focuses at the outer edge of the mirror.

For the frequency of 100 cycles/diameter, the transfer functions in the t and s directions at different field positions are given in Figure 14. The analysis of the edge diffraction can be evaluated using the T field curve. For the 4.2 m parabola, the diffracted edge ratio, defined as Eq.(3) is shown in Figure 15. The difference of the T field curve at the outer and inner edges is 46 mm. The image size is 19.8 mm radius, so the diffracted edge ratio at the inner edge is 3.6% when the interferometer focuses the outer edge. This ratio is the same at the outer edge when the interferometer focuses the inner edge. As the interferometer focuses at different field position, the diffracted edge ratios for both the inner and outer edges are shown in Figure 15.

Downloaded from SPIE Digital Library on 29 Sep 2011 to 128.196.206.125. Terms of Use: http://spiedl.org/terms

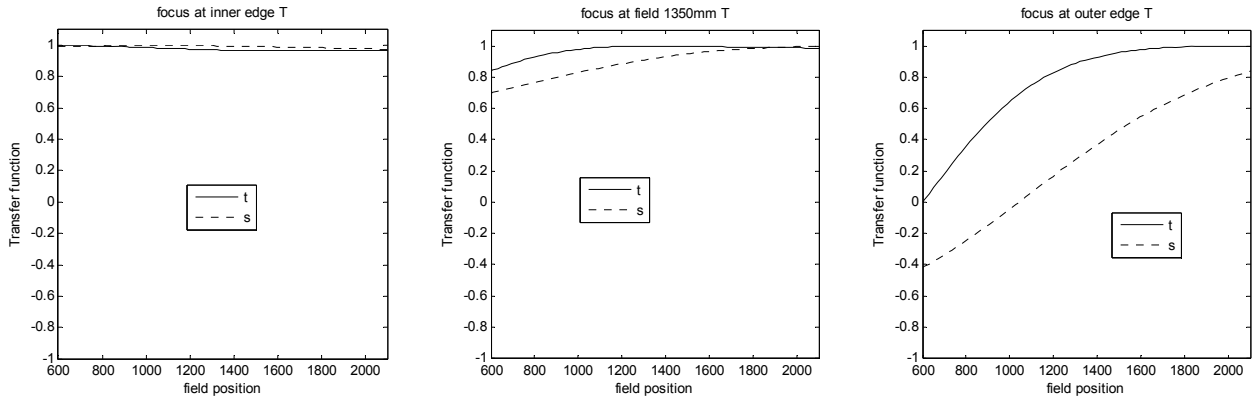

Figure 14. For 100 cycles/diameter, the transfer functions in the t and s directions at different field positions.

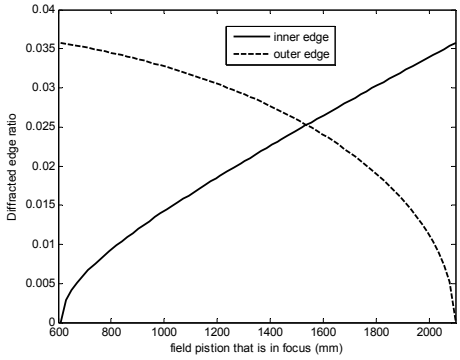

Figure 15. The diffracted edge ratio as a function of the focus.

6. Conclusion

We show specifically how the imaging properties of CGH null correctors couple with diffraction to cause measurement errors. Using the test of a 4.2-m diameter mirror as an example, we show how these effects are mitigated by balancing the field curves due to the phase curvatures with the magnification variations. If the system focus is set to the inside edge of the mirror under test, then the fact that the outer edge is defocused for both principal directions is balanced with the increased magnification that makes the features on the mirror appear proportionally larger.

REFERENCE

[1] D. Malacara, Optical Shop Testing, 2nd ed. Wiley (1992).

[2] L. A. Selberg, "Interferometer accuracy and precision", Proc. SPIE **1400**, 24-32 (1990)

[3] P. E. Murphy, T. G. Brown, and D. T. Moore, "Measurement and calibration of interferometric imaging aberrations," Applied Optics Vol.39, No.34, 6421-6429 (2000)

[4] C. Zhao and J. H. Burge, "Orthonormal vector polynomials in a unit circle application: fitting mapping distortions in a null test," Proc. SPIE **7426**, (2009).

[5] C. Zhao, and J. H. Burge, "Imaging aberrations from null correctors," Proc. SPIE **6723**,67230L (2007)

[6] P. Zhou, J. H. Burge and C, Zhao, "Diffraction effects for interferometric measurements due to field aberrations," to be submitted to Optics Express (2010).

[7] P. Zhou and J. H. Burge, "Limits for interferometer calibration using the random ball test," Proc. of SPIE **7426**, 74260U (2009).

[8] P. Zhou and J. H. Burge, "Analysis of wavefront propagation using the Talbot effect," submitted to Applied Optics (2010).

[9] J. Goodman, *Introduction to Fourier Optics*, Roberts and Company Publisher, 88-91 (2005).

[10] J. H. Burge, "Advanced techniques for measuring primary mirrors for astronomical telescopes," PhD dissertation, University of Arizona, Tucson, AZ (1993)

[11] C. Zhao and J. H. Burge, "Generalized Coddington equations for refractive/diffraction hybrid surfaces," SPIE IODC (2010).

Downloaded from SPIE Digital Library on 29 Sep 2011 to 128.196.206.125. Terms of Use: http://spiedl.org/terms